

MIT Open Access Articles

On-orbit radiometric validation and field-of-view calibration of spaceborne microwave sounding instruments

The MIT Faculty has made this article openly available. **Please share** how this access benefits you. Your story matters.

Citation: Blackwell, William J. et al. "On-orbit radiometric validation and field-of-view calibration of spaceborne microwave sounding instruments." Microwave Remote Sensing of the Atmosphere and Environment VI. Noumea, New Caledonia: SPIE, 2008. 71540A-12. © 2008 SPIE

As Published: <http://dx.doi.org/10.1117/12.804948>

Publisher: Society of Photo-optical Instrumentation Engineers

Persistent URL: <http://hdl.handle.net/1721.1/52596>

Version: Final published version: final published article, as it appeared in a journal, conference proceedings, or other formally published context

Terms of Use: Article is made available in accordance with the publisher's policy and may be subject to US copyright law. Please refer to the publisher's site for terms of use.



On-orbit radiometric validation and field-of-view calibration of spaceborne microwave sounding instruments

William J. Blackwell, Laura J. Bickmeier, Laura G. Jairam, and R. Vincent Leslie

MIT Lincoln Laboratory, 244 Wood St., Lexington, MA, USA

ABSTRACT

Two calibration/validation efforts planned for current and future spaceborne microwave sounding instruments will be presented. First, the NPOESS Aircraft Sounder Testbed-Microwave (NAST-M) airborne sensor is used to directly validate the microwave radiometers (AMSU and MHS) on several operational satellites. Comparison results for underflights of the Aqua, NOAA, and MetOp-A satellites will be shown. Second, a potential approach will be presented for on-orbit field-of-view (FOV) calibration of the Advanced Technology Microwave Sounder (ATMS). A variety of proposed spacecraft maneuvers that could facilitate the characterization of the radiometric boresight of all 22 ATMS channels will be discussed.

Radiance observations from the NAST-M airborne sensor can be used to directly validate the radiometric performance of spaceborne sensors. NAST-M includes a total of four spectrometers, with three operating near the oxygen lines at 50–57, 118.75, and 424.76 GHz, and a fourth spectrometer centered on the water vapor absorption line at 183.31 GHz. All four feedhorns are co-located, have 3-dB (full-width at half-maximum) beamwidths of 7.5° (translating to 2.5-km nominal pixel diameter at nadir incidence), and are directed at a single mirror that scans cross-track beneath the aircraft with a nominal swath width of 100 km. We will present results for two recent validation efforts: 1) the Pacific THORpex (The Observing-system Research and predictability experiment) Observing System Test (PTOST 2003, Honolulu, HI) and 2) the Joint Airborne IASI Validation Experiment (JAIVEx 2007, Houston, TX). Radiance differences between the NAST-M sensor and the Advanced Microwave Sounding Unit (AMSU) and the Microwave Humidity Sensor (MHS) were found to be less than 1K for most channels. Comparison results for ocean underflights of the Aqua, NOAA, and MetOp-A satellites are shown.

We also present an approach for on-orbit FOV calibration of the ATMS satellite instrument using vicarious calibration sources with high spatial frequency content (the Earth's limb, for example). The antenna beam is slowly swept across the target of interest and a constrained deconvolution approach is used to recover antenna pattern anomalies. Various proposed spacecraft maneuvers will be considered, with the intent to illustrate how each maneuver will help to identify and characterize possible FOV artifacts. Radiative transfer simulations that quantitatively assess the benefit of each satellite maneuver will also be presented.

1. INTRODUCTION

In this work we use inter-sensor comparisons to assess the accuracy of microwave satellite radiometers. Radiance observations from the NAST-M airborne sensor^{1,2} are collected during satellite underflights and directly compared to radiometric measurements made by the spaceborne instruments coincident overhead. Comparison results for underflights of the Aqua, NOAA-16, NOAA-17, and MetOp-A satellites follow. Specifically, radiance-to-radiance data comparisons from two campaigns are presented: 1) the Pacific THORpex (The Observing-system Research and predictability experiment) Observing System Test (PTOST 2003, Honolulu, HI) and 2) the Joint Airborne IASI Validation Experiment (JAIVEx 2007, Houston, TX).

E-mail: wjb@ll.mit.edu, Telephone: 1 781 981 5324

This work was sponsored by the National Oceanic and Atmospheric Administration under Air Force contract FA8721-05-C-0002. Opinions, interpretations, conclusions, and recommendations are those of the authors and not necessarily endorsed by the United States Government.

2. METHODOLOGY FOR INTER-COMPARISONS OF NAST-M AND AMSU/MHS

2.1. The NAST-M Airborne Instrument

NAST-M is a multi-channel passive microwave sounder. It flies alongside its sister sensor NAST-I, an IR interferometer. Together they make up the NPOESS Aircraft Sounder Testbed (NAST). The NAST instrument suite is typically mounted on NASA high altitude research aircraft as shown in Fig. 1, and is used in support of a variety of research programs.

The NAST-M sensor comprises a total of four spectrometers, with three operating near the oxygen lines at 50–57, 118.75, and 424.76 GHz, and a fourth spectrometer centered on the water vapor absorption line at 183.31 GHz. The NAST-M 54-GHz spectrometer has five channels matching corresponding AMSU-A channels, and the 183-GHz spectrometer has three channels matching corresponding AMSU-B and MHS channels. This spectral coincidence enables direct radiance-to-radiance comparisons, circumventing potential pitfalls and modeling errors that can be introduced when radiosonde or Numerical Weather Prediction profiles are used to simulate on-orbit satellite radiometers. Additional NAST-M channels near 118.75 and 424.76 can be used to further improve the fidelity of the radiometric calibration analyses. All four of NAST-Ms feedhorns are co-located, and have 3-dB (full-width at half-maximum) beamwidths of 7.5°, which translates to approximately 2.5-km nominal pixel diameter at nadir incidence. The four feedhorns are directed at a single mirror that scans cross-track beneath the aircraft, spanning ± 65 degrees. The NAST-M sensor package is mounted on an aircraft platform with a typical cruising altitude of 17–20 km, which results in a nominal swath width of 100 km. This high-altitude mobile platform enables good spatial and temporal coincidence with satellite measurements, and NAST-Ms 100 km swath width provides complete coverage of both AMSU and MHS nadir footprints (AMSU-A, AMSU-B, and MHS nadir footprints are 50 km, 15 km, and 15 km, respectively.) NAST-M also flies with additional instrumentation to aid post-collection data analysis. For example, it has a nadir-viewing video camera that collects video images during each flight. These video images can be used later to help assess the cloud levels present at the time of NAST-M data collection. They can also be used to confirm the surface type over which specific data swaths were collected (i.e. land versus ocean).

2.2. NAST-M Calibration

Reliable calibration of NAST-Ms radiometers is essential to its use as a validation sensor. NAST-M observations are calibrated using a three point calibration scheme. As the aircraft flies forward, NAST-Ms internal scanning reflector rotates. With each full rotation, the reflector captures incoming radiation from nadir viewing and three thermal sources of known temperature. The arrangement of scanning reflector with respect to the thermal sources is shown in Fig. 2. A linear fit of the voltage returns from the three thermal sources is used to convert target data voltage counts to brightness temperatures. This linear fit is illustrated in Fig. 2b, and the linear equation is shown in (1), where g is gain or slope, c is counts, and b is the baseline offset.

$$T_B = g \times c + b \quad (1)$$

2.3. Atmospheric Correction

As illustrated in the idealized NAST-M underflight depicted in Fig. 3, the NAST-M sensor and satellite fly at significantly different altitudes and each has its own distinctive swath geometry. To address these differences, two types of atmospheric corrections are applied before the satellite and NAST-M datasets are directly compared. First a limb correction is estimated for each sensors off-axis footprints using radiative transfer simulations [3] [4] based upon the best atmospheric profile available. This correction accounts for the effects of longer atmospheric path lengths seen by off-nadir footprints, and is generated for and applied to both the satellite and the NAST-M data. An altitude correction must also be applied to the NAST-M data to correct for atmospheric path length differences due to the difference in altitude between NAST-M and the satellite. This correction is also simulated using the best atmospheric profile available for each datasets geographic location and time.

Since both of these simulated corrections are generated based on an atmospheric profile, it is important to use a profile that is as true-to-life as possible. Therefore, a hybrid of dropsonde, radiosonde, and numerical models are sometimes used to compile a best estimate of the atmospheric state at the time and location of data collection.

2.4. Data Co-location

Once atmospheric corrections have been applied, the two datasets are spatially aligned and down-sampled according to spatial and temporal requirements, as shown in Fig. 4. In this way, only the data with the best coincidence are compared. Typically, the temporal requirement is one hour and the geographic proximity requirement is 30 kilometers and 11 kilometers for AMSU-A and MHS, respectively. However, datasets that are especially well-aligned may enable comparison criteria that are much stricter. For example, Fig. 5 shows a collection off the coast of Kauai, HI, on March 1, 2003. On this day NAST-M flew a course that almost perfectly matched the path of the Aqua satellite passing overhead. Consequently, the temporal requirement of ± 5 minutes can be used for this inter-comparison, which represents our most highly coincident dataset from the PTOST campaign.

3. NAST-M INTERCOMPARISON RESULTS

3.1. PTOST Campaign

The PTOST campaign was conducted out of Honolulu, Hawaii in the early Spring of 2003 over the Pacific Ocean. This campaign included NAST-M underflights of NOAA-16, NOAA-17, and Aqua satellites. PTOST comparisons for AMSU-A and AMSU-B comparisons are shown in Tables 1 and 2, where μ is the mean bias estimate and σ is the standard deviation of the bias estimate. Video images were used as a cloud reference during post-processing of PTOST data. In particular, these images confirmed the presence of clouds during the March 11, 2003 collection, helping to explain the increased radiometric deviation observed in window channels for that day. For other collections, such as March 12, the video images confirmed the presence of clear air. Fig. 6 shows examples of video images at the time of NAST-M data collection for March 11 and March 12.

3.2. JAIVEx Campaign

The JAIVEx campaign was conducted out of Houston, Texas in the spring of 2007 over the Gulf of Mexico. JAIVEx comparisons for AMSU-A and MHS sensors on the METOP-A satellite are shown in Table 3. The NAST-M data collection on April 20th, 2007 occurred at night, so video data was not helpful in assessing the presence of clouds.

3.3. Discussion and Conclusions

This comprehensive study compared NAST-M data to multiple satellites under a variety of atmospheric conditions and in two geographic locations. Biases between NAST-M and AMSU sensors were observed to be less than 1K for most channels. Improvement of NAST-M calibration is an ongoing effort. In future work, we plan to include in our analysis additional data over a variety of surface types.

4. ON-ORBIT FIELD-OF-VIEW CALIBRATION OF ATMS

4.1. ATMS background and status

The ATMS flight unit for NPP (launch in the 2010–2011 timeframe) was delivered in 2005. Radiometrically, ATMS is well-characterized through pre-launch testing, and antenna pattern measurements indicated no major problems. However, similar pre-launch testing procedures revealed no issues during AMSU pre-launch characterization, while angle-dependent biases greater than 2K have been observed for every AMSU sensor that has launched—an example is shown in Fig. 7. This can be explained by three factors. First, antenna pattern testing is substantially inaccurate in the far sidelobe regions in the high frequency regions (greater than 60 GHz) due to limitations of the testing equipment and environment. Second, the antenna system under test does not accurately reflect the on-orbit mission-nominal flight configuration of the sensor, as only the antenna subassembly was tested – emissive and reflective properties of the sensor exterior and spacecraft environment were not directly assessed. Third, the antenna pattern testing did not evaluate all Earth scene positions and only measured a finite number of cuts (usually four) through the two-dimensional spatial response function (SpaRF).

An on-orbit spacecraft maneuver could provide valuable assessments of the ATMS SpaRF at all beam positions, at accuracies substantially exceeding those possible with pattern measurements, at conditions closely resembling mission-nominal. We describe some possible scenarios and present analysis simulations below.

4.2. Simulation of an ATMS scan of the Earth's limb using spacecraft maneuvers

With knowledge of the atmospheric state, the antenna pattern can be recovered with the following procedure. First, the antenna beam is slowly swept across the Earth's limb. Second, radiometric measurements as a function of pitch and roll are taken as the satellite is rotated. Finally, the RMS error between measurements and simulations is minimized by fitting a first guess pattern function to the measurements and optimizing free parameters such as: sidelobe location(s), width(s), and amplitude(s).

A radiative transfer simulation environment was constructed to accurately model the radiometric signatures that will be observed by ATMS during the spacecraft maneuvers. The major components are shown in Fig. 8. The following assumptions are made: the surface temperature and emissivity are uniform (resembling an ocean surface), the atmospheric state is represented by the 1976 US Standard Atmosphere, and the atmosphere is spherically stratified and horizontally homogeneous. These assumptions yield an azimuthal symmetry with respect to the satellite zenith angle and greatly simplify the required spatial convolution of the two-dimensional brightness temperature field with the spatial response function. The FASTEM emissivity model was used with the MIT TBARRAY radiative transfer model to simulate the ATMS observations as a function of sensor scan angle.

As each field-of-view is scanned across the Earth's limb, a pronounced drop in the brightness temperature will occur as the cosmic background ($\sim 2.7\text{K}$) enters the field-of-view (at a viewing angle of approximately 62° assuming a satellite altitude of $\sim 830\text{km}$). The angular distributions of brightness temperatures resulting from this simulation are shown in Fig. 9 and show the precipitous drop in brightness temperature at the Earth's limb. The ATMS observations can be expressed as the convolution of the brightness temperature distribution (known) and the antenna pattern (unknown). The antenna pattern can therefore be recovered by deconvolving the observations and the known brightness temperature distribution. This idealized recovery technique is difficult in practice because both the antenna pattern and the brightness temperature field vary in two dimensions, and the deconvolution procedure is inherently noisy. A priori information about the antenna pattern can be used to constrain the solution to tend toward the a priori pattern features. This approach is used in this work, where a "template" antenna pattern is adjusted through the tuning of several free parameters so that the observations match the convolution of the recovered pattern and the brightness temperature field.

Open ocean is assumed for the simulations. This minimizes crosstalk from land-sea crossings and provides a uniform background. A conservative estimate of the possible global areas that could provide an ocean surface over an entire scan of the Earth's limb is shown in Fig. 10.

4.3. Recovery of ATMS antenna patterns

A nominal ATMS antenna pattern is shown in Fig. 11. To illustrate the recovery procedure for a simple, idealized case, we introduce a sidelobe to the nominal pattern at 20 degrees (down-track) at a level of -20 dB. A single roll or pitch maneuver may not be adequate to recover the sidelobe location, as certain (front-back, left-right) ambiguities cannot be resolved. An example of a positional ambiguity is shown in Fig. 11 (red curve). A two-dimensional maneuver (where separate pitch and roll maneuvers are performed separately and composited) is able to accurately recover the sidelobe position, amplitude, and width.

4.4. Discussion

We have established a simulation system and a basic sidelobe recovery algorithm that can be used to evaluate more sophisticated maneuver parameters under less ideal assumptions than were used in this study. Future plans include use of a spatially heterogeneous global atmospheric model and actual ATMS antenna pattern measurements. These improvements can be easily accommodated by the existing simulation infrastructure.

Another area of study involves an assessment of the uncertainties associated with the recovered pattern. One complicating issue is the thermal state of the radiometer will drift over the course of the maneuver and this may slightly alter the radiometric transfer function. The radiometer gain and offset will be calibrated periodically, but small changes in nonlinearity, for example, could introduce errors in the recovery process. An error model is under development based on pre-launch thermal vacuum data that were observed over a range of sensor operating conditions, and this model will be used to estimate the on-orbit uncertainties that could be encountered.

Acknowledgments

This work was supported through the NPOESS Integrated Program Office Internal Government Studies Program.

REFERENCES

1. W. J. Blackwell, J. W. Barrett, F. W. Chen, R. V. Leslie, P. W. Rosenkranz, M. J. Schwartz, and D. H. Staelin, "NPOESS aircraft sounder testbed-microwave (NAST-M): Instrument description and initial flight results," *IEEE Trans. Geosci. Remote Sensing* **39**, pp. 2444–2453, November 2001.
2. R. V. Leslie and D. H. Staelin, "NPOESS aircraft sounder testbed-microwave: Observations of clouds and precipitation at 54, 118, 183, and 425 GHz," *IEEE Trans. Geosci. Remote Sensing* **42**, pp. 2240–2247, October 2004.

Table 1
AMSU-A PTOST Bias Estimates

Satellite Date GHz	NOAA-16 3/11/03		NOAA-17 3/12/03		Aqua 3/1/03		Aqua 3/3/03	
	μ	σ	μ	σ	μ	σ	μ	σ
50.3	4K*	±7K	-1.7K	±1.1K	-0.38K	±0.9K	-0.45K	±1.3K
52.8	2.2K*	±1.3K	1.1K	±0.2K	1.86K	±0.1K	2K	±0.3K
53.75	-0.6K	±0.3K	-0.5K	±0.1K	0.06K	±0.4K	0.37K	±0.2K
54.4	0.64K	±0.2K	0.6K	±0.3K	0.65K	±0.3K	0.52K	±0.3K
54.94	0.4K	±0.2K	0.36K	±0.3K	N/A†		N/A†	
55.5	0.2K	±0.3K	-0.8K	±0.1K	0.17K	±0.2K	0.01K	±0.3K

* This was a very cloudy day, which increases variation in window and humidity channels

† Aqua channel 54.9GHz was disregarded due to excessive sensor noise

Table 2
AMSU-B PTOST Bias Estimates

Satellite Date GHz	NOAA-16 3/11/03		NOAA-17 3/12/03	
	μ	σ	μ	σ
183.3±1.0	4.2K*	±0.6K	-2.9K	±1.7K
183.3±3.0	1.2K*	±0.7K	-0.2K	±1.4K
183.3±7.0	2K*	±1.0K	-0.9K	±2K

Table 3
AMSU-A JAIVEx Bias Estimates MHS JAIVEx Bias Estimates

Satellite Date GHz	METOP-A 4/20/07	
	μ	σ
50.3	-0.8K	±0.4K
52.8	0.9K	±0.3K
53.75	-0.36K	±0.3K
54.4	-0.36K	±0.3K
54.94	-0.15K	±0.6K
55.5	-1.5K	±0.5K

Satellite Date GHz	METOP-A 4/20/07	
	μ	σ
183.3±1.0	1K	±0.7K
183.3±3.0	N/A§	
183.3+7.0	1.4K	±0.4K

§NAST-M channel not operational for this flight

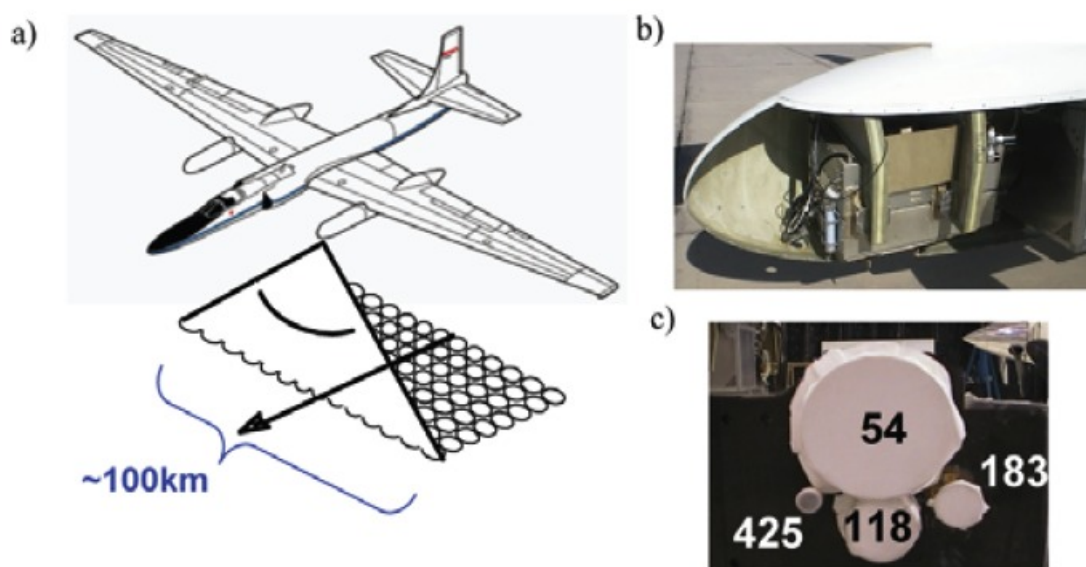


Figure 1. a) Sketch of NPOESS Aircraft Sounder Testbed (NAST), b) The NAST-M sensor mounted in a wing pod onboard the aircraft, c) The four NAST-M radiometers.

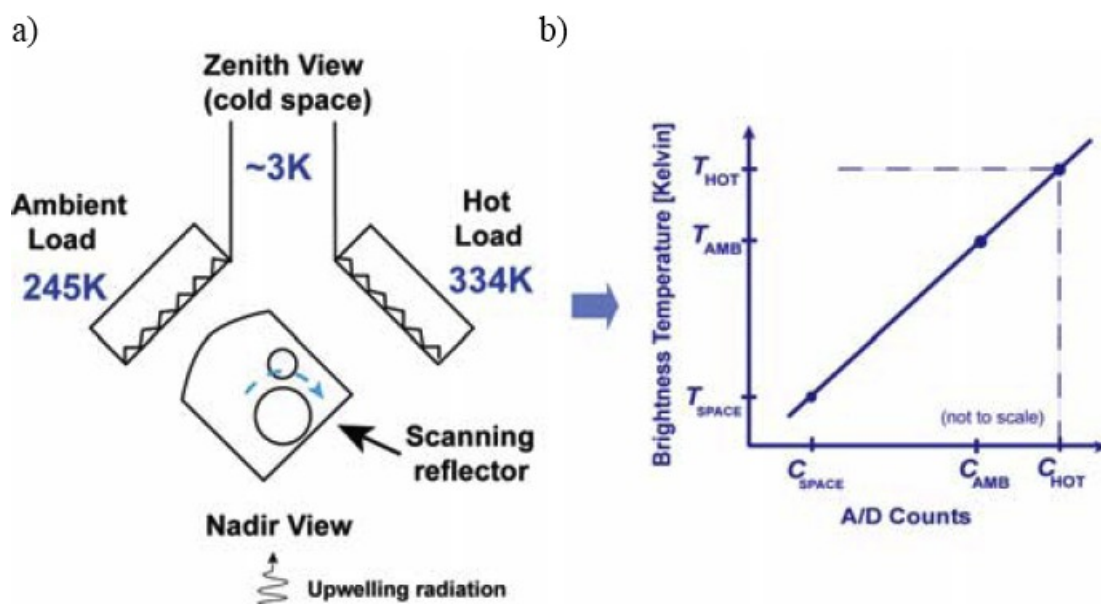


Figure 2. a) NAST-M reflector and calibration load schematic. Aircraft velocity vector is into the page. b) Each sweep of the scanning reflector measures upwelling emission from the scene views, followed by observations of the three thermal loads of known temperature, which are used to calibrate the radiometer.

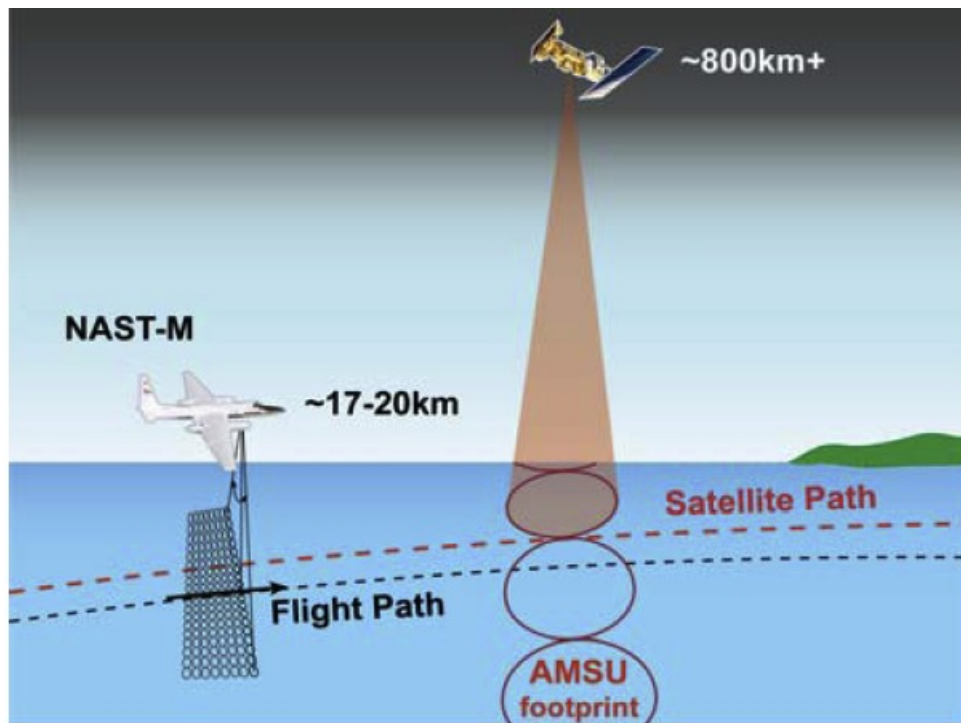


Figure 3. A drawing of an idealized NAST-M underflight of a satellite. Drawing is not to scale.

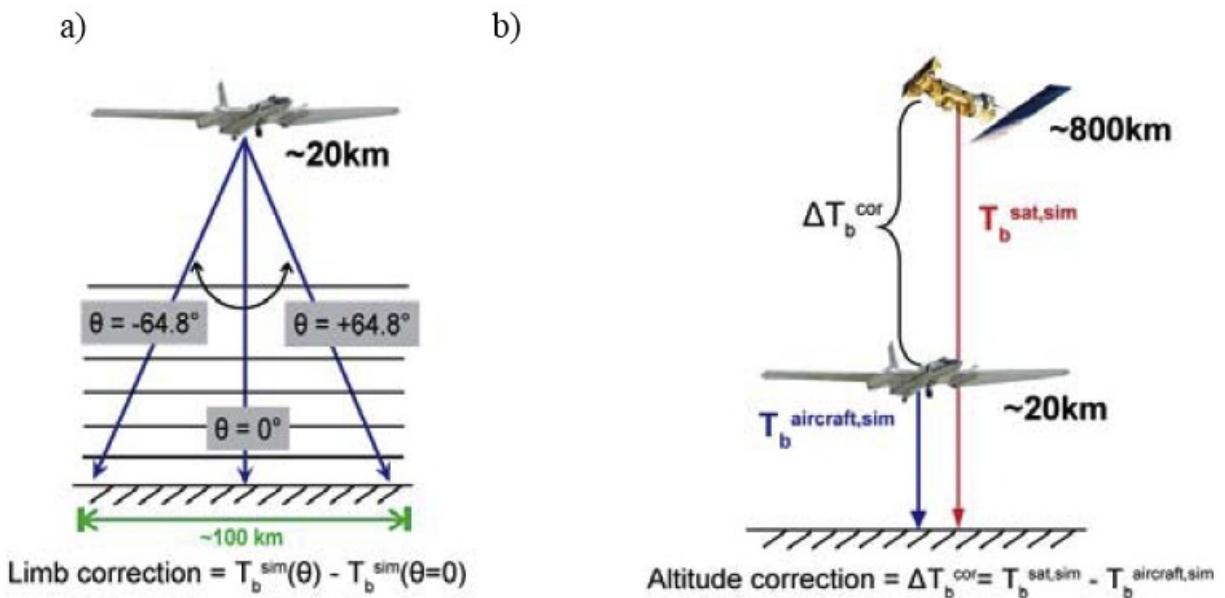


Figure 4. a) Limb corrections for off-nadir data and b) altitude corrections for NAST-M data are generated using RTM simulations. These images are not to scale.

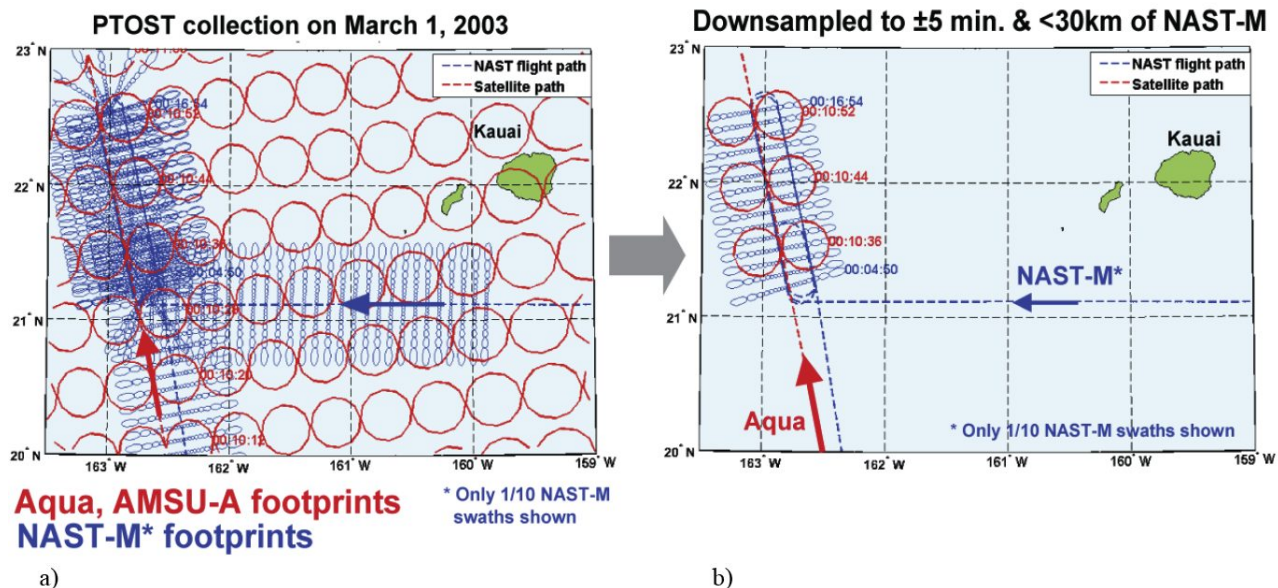


Figure 5. Example of a data down-sampling using March 1st, 2003 collection a) before down-sampling, and b) after down-sampling.

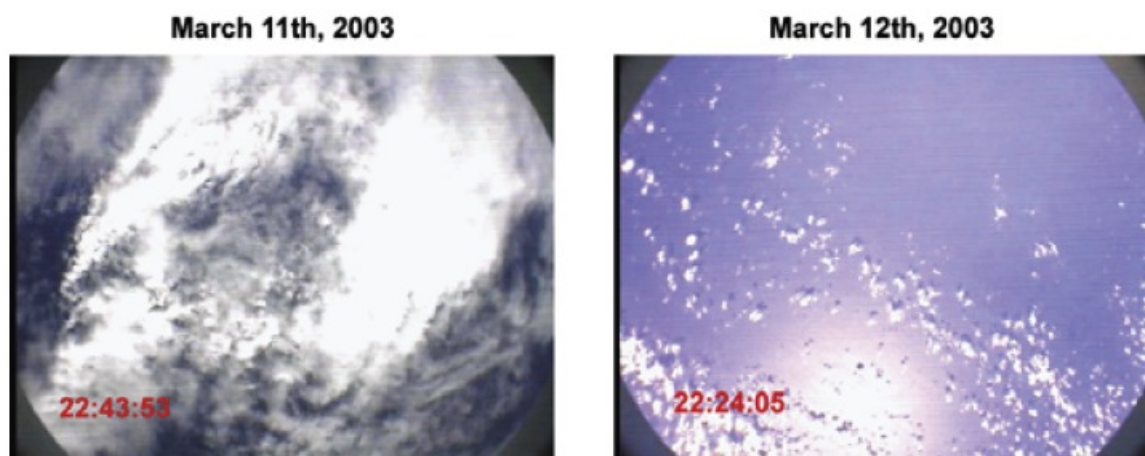


Figure 6. Example video images for March 11th, 2003 and March 12th, 2003. Video images captured during the PTOST collections were used to help assess cloud impact on the data.

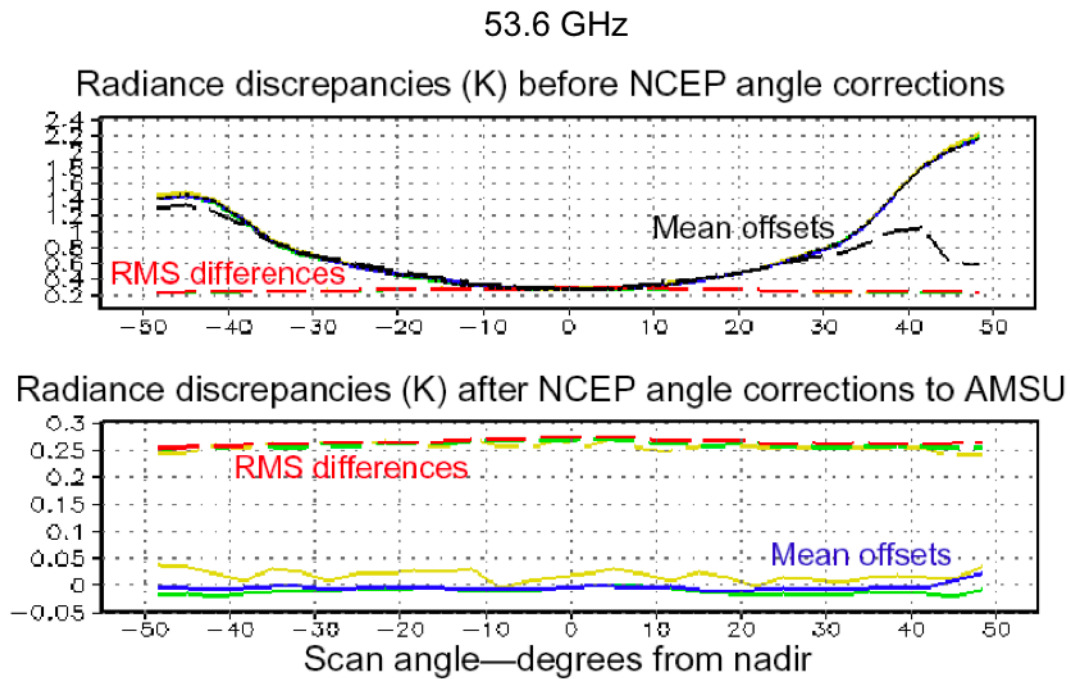


Figure 7. Global comparisons of AMSU-A (Aqua) observations with NCEP model versus scan angle. Figure courtesy of NOAA/NESDIS.

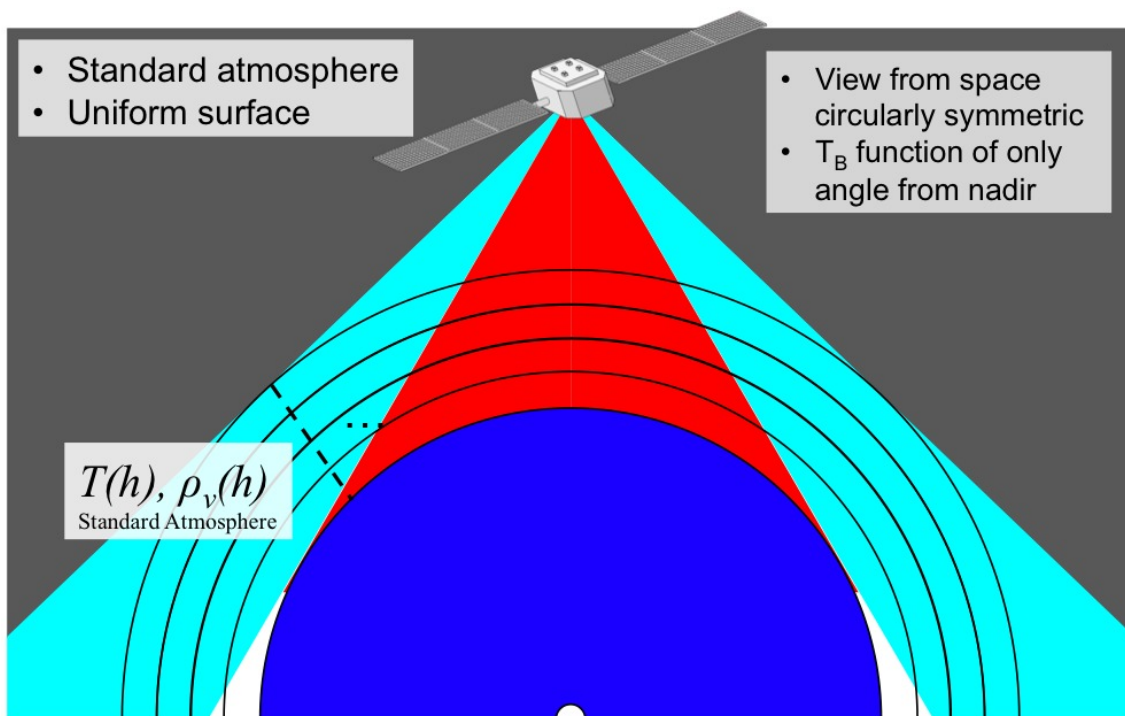


Figure 8. Spherically-symmetric model of the Earth's atmosphere and limb.

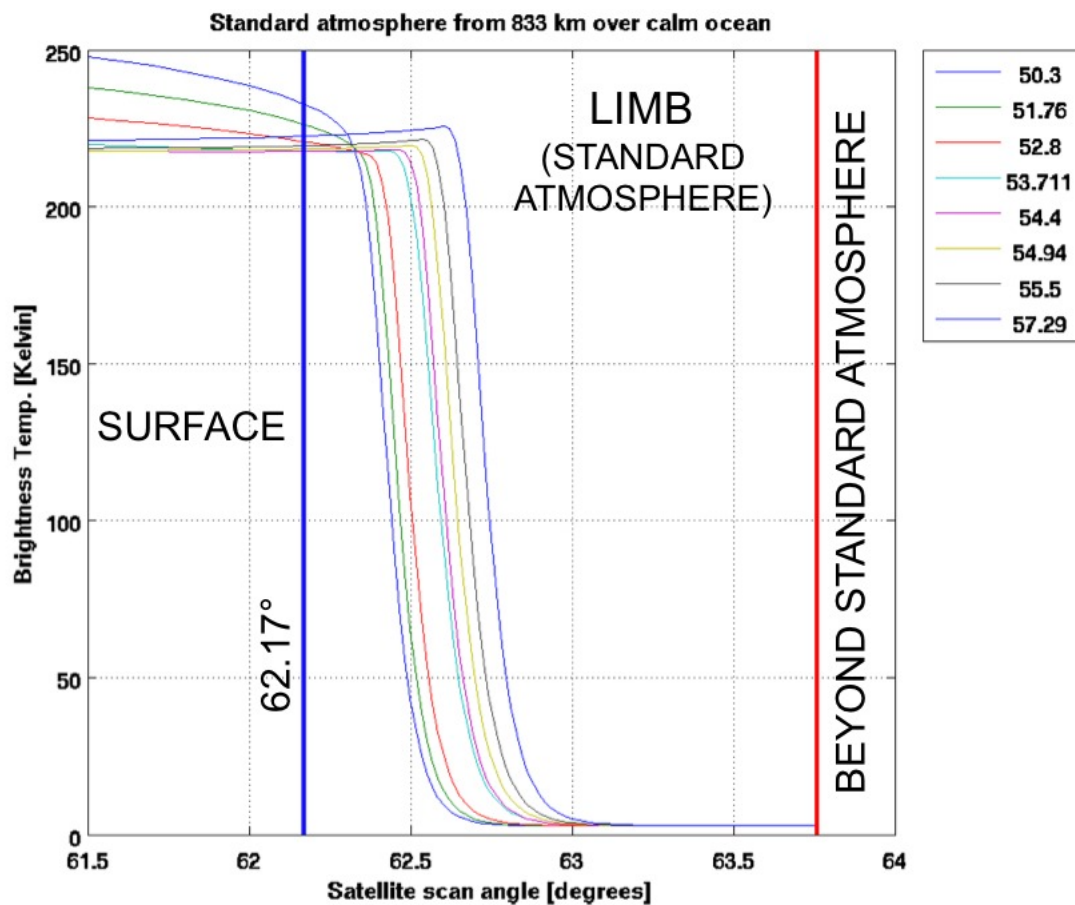


Figure 9. Atmospheric “source functions” are convolved with the (unknown) ATMS antenna pattern.

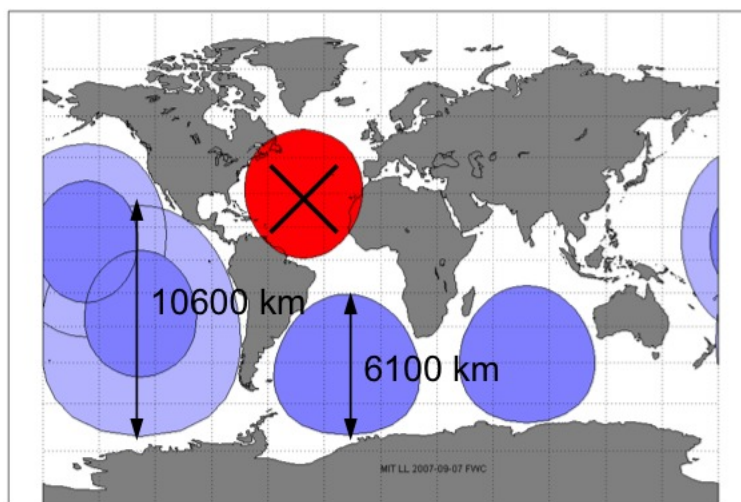


Figure 10. Area projections on the Earth's surface for which ocean view is subtended out to the limb.

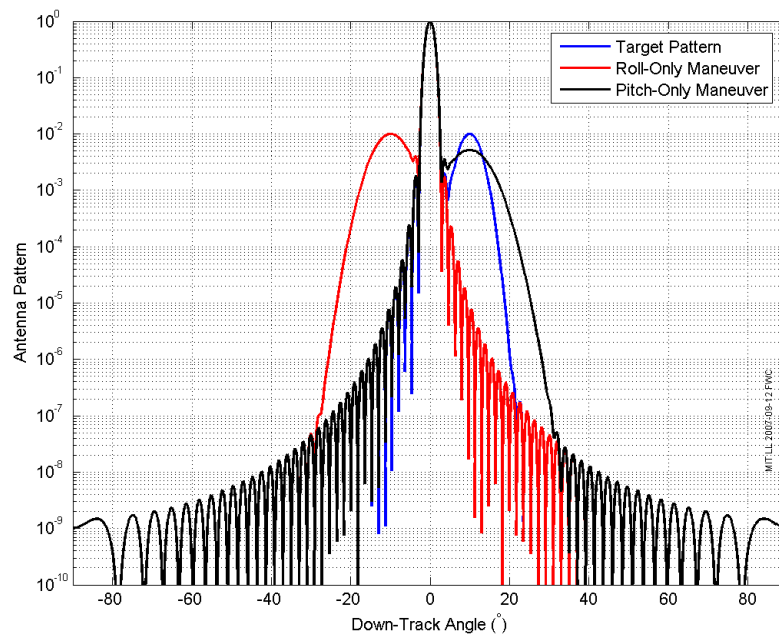


Figure 11. One-dimensional maneuvers could fail to resolve ambiguities in the location of sidelobe anomalies.

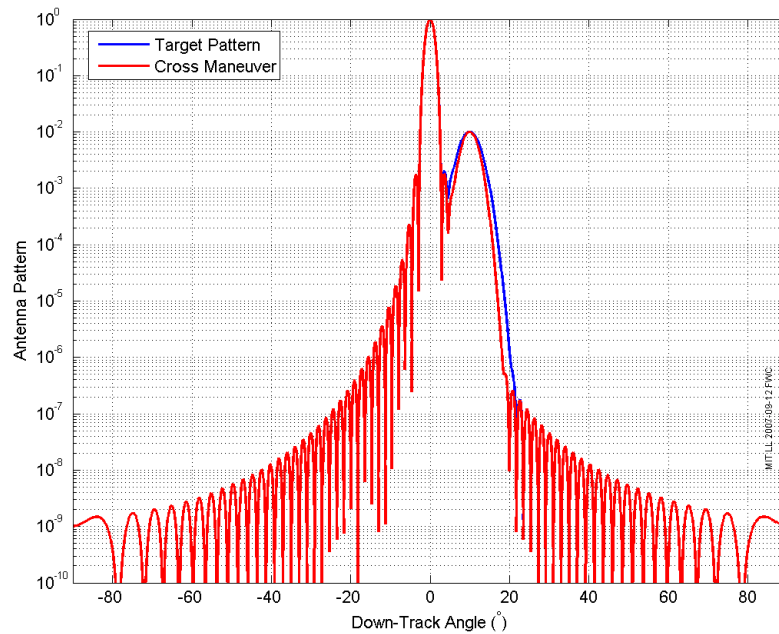


Figure 12. Two-dimensional maneuvers allow accurate recovery of sidelobe position, width, and amplitude.